Identification of the effective interface between the homogenized phases of a dual-weave 3D composite

Léonard Turpin, Jan Neggers, Arturo Mendoza, Julien Schneider, Yannick Pannier, Stéphane Roux

▶ **To cite this version:**

Léonard Turpin, Jan Neggers, Arturo Mendoza, Julien Schneider, Yannick Pannier, et al.. Identification of the effective interface between the homogenized phases of a dual-weave 3D composite. European Journal of Mechanics - A/Solids, 2024, 103, pp.105166. 10.1016/j.euromechsol.2023.105166 . hal-04267051

HAL Id: hal-04267051
https://hal.science/hal-04267051

Submitted on 1 Nov 2023

HAL is a multi-disciplinary open access archive for the deposit and dissemination of scientific research documents, whether they are published or not. The documents may come from teaching and research institutions in France or abroad, or from public or private research centers.

L'archive ouverte pluridisciplinaire **HAL**, est destinée au dépôt et à la diffusion de documents scientifiques de niveau recherche, publiés ou non, émanant des établissements d'enseignement et de recherche français ou étrangers, des laboratoires publics ou privés.

Identification of the effective interface between the homogenized phases of a dual-weave 3D composite

Léonard Turpin[a,*], Jan Neggers[a], Arturo Mendoza[a,b], Julien Schneider[c], Yannick Pannier[d], Stéphane Roux[a]

[a] *Univ. Paris-Saclay/CentraleSupélec/ENS Paris-Saclay/CNRS, LMPS — Laboratoire de Mécanique Paris-Saclay, F-91190, Gif-sur-Yvette, FRANCE*
[b] *Safran Tech, F-78117, Châteaufort, FRANCE*
[c] *Safran Aircraft Engine, F-77550, Moissy-Cramayel, FRANCE*
[d] *Univ. de Poitiers/ISAE-ENSMA/CNRS, Institut PPRIME F-86960, Chasseneuil Futuroscope, FRANCE*

Abstract

Hybridization enhances composite properties by assembling several reinforcement materials. In woven composites, the distribution of different yarns can induce a macroscopic heterogeneity in the thermomechanical properties, which can be considered in the modeling through the introduction of homogenized phases regionally. Identifying the interfaces between those effective phases based on the geometry is difficult due to the yarn entanglement at the interfaces. This work proposes to identify the optimal positions of interfaces by observing the global mechanical behavior of the composite. An asymmetric glass/carbon-hybrid 3D-interlock fabric is studied. It results in a dual-weave composite modeled as macroscopically bi-phased material. It is shown that the effective interface position can be determined from a heating-cooling experiment tomographied in-situ, and processed by Integrated Digital Volume Correlation (IDVC), together with some of the thermomechanical properties of each phase. To enhance IDVC

*Corresponding author, current address: Diamond Light Source, Harwell Science & Innovation Campus, Dicdcot, OX11 0DE, UK
Email address: leonard.turpin@diamond.ac.uk (Léonard Turpin)

sensitivity, a specific procedure is designed to include the specimen boundary in the analysis.

Keywords: Organic Matrix Composite (OMC), Integrated Digital Volume Correlation (IDVC), homogenization, in-situ thermal experiment

---

1. Introduction

The architecture of fiber reinforced composite materials is optimized considering their expected local loading states [1, 2, 3]. Hybridization consists in combining several reinforcement materials [4]. Hybrid laminate composites are made of layered UD [5] or 2D-woven [6, 7] plies of different nature and have a high impact resistance. While layered composites are prone to delamination [8], 3D reinforcements — using Z-yarn reinforcements [9, 10] or an interlock fabric [11] — limit this phenomenon. The distribution of the different kinds of fibers depends on the applications and can be homogeneous [11], heterogeneous and symmetric [6], or heterogeneous and asymmetric [10].

Thermomechanical models have to take into account the effect of the hybridization to reproduce the composite behavior accurately. Those models are usually finite-element (FE) analyses, including homogenization hypotheses. While mesoscale modeling [12] can be used for the hybridisation of 3D woven composites, the industrial applications tend to favor simpler models. Indeed, mesoscale models that describe the complete mesostructure with the required level of detail are very costly to obtain (*e.g.* via tomography of the material during the fabrication process [13] or simulation of the weaving process [14]). Moreover, the number of degrees of freedom required to describe large parts becomes prohibitive. It is generally more relevant to consider a model with only few macroscopic phases with their own properties and orientation [15]. The difficulty is then to determine the position of the interfaces between those homogenised phases. In most cases, typically for 3D-interlock weaving presenting yarn entanglements at the interfaces, there are no physical boundaries between those phases, and an interface based on the geometry is not the most suitable.

A *mechanically-based* interface can then be defined as the interface for which the model reproduces the mechanical behavior of the sample at best.

During operation, structural parts of airplanes can be submitted to substantial temperature changes, typically from -50°C to 90°C [16]. The experiment used for the interface identification procedure applies a similar temperature cycle to mimic the thermal loading during a flight. The sample, extracted from a structural aeronautical part, consists in an asymmetric hybrid 3D-interlock composite. On one side, it is composed of carbon yarns only; on the other side, of glass warp yarns and carbon weft yarns. The textile is embedded in an epoxy resin matrix. During the experiment, it mostly displays a bimetal effect, *i.e.* bending induced by a differential thermal dilatation. Thus the interface position influences the deformed shape of the sample. The strain amplitude at the sample surfaces is low and is decorated by high-frequency modulation at the weaving scale (a few millimeters). Measuring the overall bending of the sample by conventional methods, *e.g.* strain gauges [17], is therefore difficult.

This article proposes an identification procedure to determine the best mechanically-based interface from an in-situ thermo-mechanical experiment.

It was chosen to provide a methodology that could be applied to a more complex interface or sample geometries. The thermal dilatation creates strain incompatibilities, resulting in a complex deformation and stress distribution, requiring a full-field measurement procedure, as Digital Image Correlation (DIC) [18, 19]. The heterogeneity of the material induces a 3D kinematics. Digital Volume Correlation (DVC) [20, 21, 22] is then particularly well-suited. The thermal cycle experiment is followed by tomography. The texture of the tomographic images — resulting from the heterogeneity of the material constituents — is used for DVC. The texture is not uniformly distributed, namely between the two phases. Moreover, the low strain level is experimentally challenging due to the high measurement uncertainty typical for X-ray tomography images which often contain strong noise and reconstruction artifacts (*e.g.* rings, beam hardening, scattering) that impact both DVC [23] and the identification procedure [24]. A good way to reduce the impact of noise and texture het-

erogeneities is to reduce the number of parameters to identify, integrating the model into the identification procedure, resulting in so-called Integrated Digital Volume Correlation (IDVC) [23, 25, 26]. The novelty of this work is to use IDVC not only for identifying material parameters but also for identifying geometrical parameters defining the interface.

Section 2 describes the in-situ heating-cooling experiment on a parallelepipedic sample made of glass and carbon yarns and an epoxy matrix. Section 3 recalls the basics of IDVC. The identification procedure is explained in Section 4. The results are summarized in Section 5, and Section 6 offers considerations about the quality of the identified interface and the tuned model. Eventually, some perspectives are proposed in Section 7.

2. Sample and experiments

The sample is an asymmetric hybrid interlock composite. It is a $22 \times 6 \times 40\,\mathrm{mm}^3$ hexahedron. The fabric is made of carbon and glass yarns (Fig. 1a and 1b): on one side of the sample, warp and weft yarns are made of carbon fibers; while on the other side, warp yarns are made of glass fibers and weft yarns of carbon fibers. The weaving architecture is the same. Each yarn is composed of only one kind of fiber, and the epoxy matrix is injected into the fabric by Resin Transfer Molding (RTM). The fiber volume fraction is 60%.

This material can be considered biphasic at the macroscopic scale (Fig. 1c). In the Finite-Element (FE) model, each phase is a homogeneous orthotropic thermoelastic material [27, 28]. The *carbon-carbon* phase properties are known from experiments on "macroscopically monophasic" samples with an equivalent woven structure. The initial properties of the *glass-carbon* are adapted from the properties of the carbon-carbon, changing the values in the direction of the glass yarns (warp orientation). Table 1 summarizes the corresponding properties.

The geometrical position of the flat planar interface between the two phases is determined considering the number of layers of each type of yarn: three glass-carbon and five carbon-carbon (Fig. 1a). The interface is naturally assumed to

material	description	param.	initial	identified	uncertainty
glass-carbon	Young's moduli	E_{11} (GPa)	26.6	43.2	0.7
		E_{22} (GPa)	59.6	60.5	1.5
		E_{33} (GPa)	9.2	4.4	0.3
	Poisson's ratios	ν_{12}	0.2	·	·
		ν_{13}	0.3	·	·
		ν_{23}	0.3	·	·
	shear moduli	G_{12} (GPa)	6.1	8.3	0.2
		G_{13} (GPa)	4.5	1.5	0.07
		G_{23} (GPa)	1.3	1.5	0.04
	coefficients of	k_{11} (K^{-1})	1.2×10^{-5}	9.8×10^{-6}	3×10^{-8}
	thermal expansion	k_{22} (K^{-1})	7.0×10^{-6}	4.7×10^{-6}	2×10^{-8}
		k_{33} (K^{-1})	2.2×10^{-5}	2.6×10^{-5}	5×10^{-8}
carbon-carbon	Young's moduli	E_{11} (GPa)	76.8	·	·
		E_{22} (GPa)	59.6	61.0	2
		E_{33} (GPa)	9.2	2.2	0.1
	Poisson's ratios	ν_{12}	0.2	·	·
		ν_{13}	0.3	·	·
		ν_{23}	0.3	·	·
	shear moduli	G_{12} (GPa)	6.1	8.5	0.2
		G_{13} (GPa)	4.5	3.3	0.2
		G_{23} (GPa)	3.7	4.2	0.2
	coefficients of	k_{11} (K^{-1})	1.5×10^{-6}	3.0×10^{-6}	2×10^{-8}
	thermal expansion	k_{22} (K^{-1})	5.2×10^{-6}	5.2×10^{-6}	2×10^{-8}
		k_{33} (K^{-1})	4.5×10^{-5}	1.6×10^{-5}	4×10^{-8}

Table 1: Initial parameter values and result of the identification by IDVC for the homogenized material parameters of the two macroscale phases of the sample. Both materials are assumed to have an orthotropic thermo-elastic behavior. Orientations 1 and 2 correspond to the warp and weft directions respectively, and orientation 3, to the thickness (resp. z, x, y in Figure 1). The procedure to obtained the identified parameters is detailed in Section 4, and the uncertainty computation, in Section 5.2.

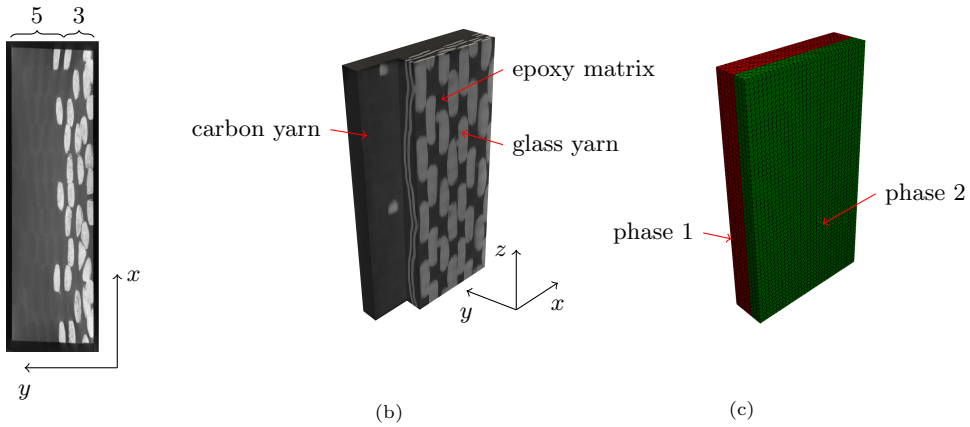

(a) (b) (c)

Figure 1: The sample (a) and (b) (resp. slice and 3D view of a tomography) is an interlock woven carbon/epoxy composite in which glass-fiber yarns replace some warp yarns. At the macro-scale, it can be modeled as a biphasic material (c). Initial Finite-Element mesh of the sample. The interface position is classically determined based on the fabric topology, respecting the ratio of glass-carbon plies (3/8).

be planar and parallel to the mean weft-warp plane.

An in-situ thermal test was carried out on this sample. The tomograph is an RX Solution *UltraTom*, located at the PPRIME Institute. A heating-cooling device (Fig. 2) applies the thermal cycle displayed in Figure 3. Four scans are acquired during the test: at 20°C, at 120°C, at −40°C, and again at 20°C (room temperature). The tomographic reconstruction and reduction of ring artifacts are performed with the commercial software *X-Act*. The beam energy is 60 keV, and exposure time is 0.1 s per frame in order to guarantee a good contrast between the glass yarns and the matrix. However, this setting leads to poor contrast between the carbon yarns and the matrix (Fig. 1a). The voxel size is $18\,\mu\mathrm{m\,vx}^{-1}$.

3. Digital Volume Correlation

3.1. DVC

Digital Volume Correlation (DVC) consists in finding the displacement field, $\boldsymbol{u}(\boldsymbol{x})$, between two images $f(\boldsymbol{x})$ and $g(\boldsymbol{x})$ minimizing the quadratic norm of the

residual, $\rho(\boldsymbol{x}, \boldsymbol{u})$ [22]

$$\rho\left(\boldsymbol{x}, \boldsymbol{u}\right) = f\left(\boldsymbol{x}\right) - g\left(\boldsymbol{x} + \boldsymbol{u}\left(\boldsymbol{x}\right)\right) \tag{1}$$

This displacement field can be expressed using a finite-element basis, $\boldsymbol{\varphi}$:

$$\boldsymbol{u}\left(\boldsymbol{x}\right) = a_i \varphi_i\left(\boldsymbol{x}\right) \tag{2}$$

The minimization is achieved using a Newton-Raphson method [29]. The incremental system becomes

$$[M]\{\delta a\} = \{b\} \tag{3}$$

with

$$\left\{ \begin{array}{rcl} [M] & = & \displaystyle\int \left(\boldsymbol{\nabla} f \boldsymbol{\varphi}\right)^\top \boldsymbol{\nabla} f \boldsymbol{\varphi} \, \mathrm{d}\boldsymbol{x} \\ \{b\} & = & \displaystyle\int \left(\boldsymbol{\nabla} f \boldsymbol{\varphi}\right)^\top \rho \, \mathrm{d}\boldsymbol{x} \end{array} \right. \tag{4}$$

with $\{\delta a\}$ the incremental correction to the displacement field.

3.2. IDVC

Integrated-DVC (IDVC), in turn, allows for the use of mechanical modeling of the displacement field [26]. The new unknowns of the problem are then the model parameters $\{p\}$. They are included in the minimization scheme thanks to their sensitivity fields $[S]$

$$\forall p_i \in \{p\}, \quad \{S_i\} = \frac{\partial \{a\}}{\partial p_i} \tag{5}$$

The incremental correction of parameters is determined solving

$$[S]^\top [M][S]\{\delta p\} = [S]^\top \{b\} \tag{6}$$

To take into account the different natures of the terms of $\{\delta p\}$, a new 2-norm $\|\delta p\|$ is defined. It involves the covariance matrix of $\{p\}$, $[\mathrm{cov}_p]$

$$\|\delta p\| = \sqrt{\{\delta p\}^\top \left[\mathrm{cov}_p\right]^{-1} \{\delta p\}} \tag{7}$$

It is dimensionless and represents the norm of the parameter vector weighted by their respective uncertainties. The covariance matrix $[\mathrm{cov}_p]$ is the inverse of the IDVC Hessian matrix, $[H]$, taking into account the noise level of the images, σ_f, and hence,

$$\left[\mathrm{cov}_p\right]^{-1} = \frac{1}{2\sigma_f^2}[H] = \frac{1}{2\sigma_f^2}[S]^\top[M][S] \tag{8}$$

As such, $\|\delta p\|$ provides a convenient convergence criterion. $\|\delta p\| < 1$ means that the incremental correction of each parameter is less than its uncertainty, which ensures stationarity of the solution.

The DVC Hessian matrix $[M]$ only depends on the reference image whereas the sensitivity fields $[S]$ depend on the loading state, and so on the time. As all the parameters to identify are not expected to vary with time, a *single* minimization is performed for the whole test. This is achieved by summing the instantaneous Hessian matrices and right-hand-side members of the two loading steps (120°C and −40°C) because the sensitivity fields for the return-to-ambient step are null (and the displacements measured by DVC are null, within uncertainty, as explained in Section 5.1).

3.3. IDVC accounting for the borders

Due to the woven structure of the sample, the *texture* supporting the DVC computation is not equally distributed inside the sample (Fig. 1a). The contrast in the glass-carbon phase is higher than in the carbon-carbon phase. The contribution of the well-textured glass-carbon phase will be dominant compared to the carbon-carbon one. The boundary of the sample handles the main information about the kinematics of the carbon-carbon phases. A way to mitigate this uneven distribution is thus to allocate a strong weight to the border of the sample. A simple and non-intrusive approach is to consider a second problem dealing only with the boundaries. Binary images are built from the tomographic

volume (0 outside the sample, 1 inside) by the mean of manual thresholding. Then, IDVC can also be performed between those images, using a pyramidal scheme [30] that progressively transitions from blurred versions of the binary images into less blurred ones. This procedure results in the best set of parameters to describe the behavior of the sample borders.

This information can be incorporated inside the identification problem by simply summing the two minimization problems. Then Equation 6 becomes

$$\begin{aligned} [S]^\top \left([M] + w_b[M_b]\right)[S]\{\delta p\} &= [S]^\top \left(\{b\} + w_b\{b_b\}\right) \\ [H_{\text{tot}}]\{\delta p\} &= \{b_{\text{tot}}\} \end{aligned} \tag{9}$$

where $[M_b]$ and $\{b_b\}$ refer to the problem considering only the borders of the sample, and $[H_{\text{tot}}]$ and $\{b_{\text{tot}}\}$ to the complete one. Moreover, w_b is the relative weight attached to the supplementary contribution of the borders. To make this factor dimensionless, w_b can be expressed as follows

$$w_b = k_b \left(\max f - \min f\right)^2 \tag{10}$$

Taking into account the dynamic range of the reference image allows the definition of an easy-to-tune parameter, k_b, that represents the relative weight between the contributions of the images of the borders and the full images.

Let us stress that DVC (and DIC) generally focuses on the inner part of the solid (surface) due to specific difficulties in handling boundaries. However, in the present case, those boundaries are extremely precious because of the poor contrast in the impregnated carbon-carbon phase. Boundaries are well defined and easy to follow, and they do not tolerate any deviation in constitutive parameters that would produce an inappropriate bending. The proposed procedure restores the missing sensitivity. One could also envision to perform a single DVC analysis with a mesh extending slightly off the sample volume. Then borders would be included in the DVC analysis naturally. One may believe this is a way to avoid the difficult question of weighting the boundary with the k_b parameter introduced above. This is unfortunately not true because the gray level outside

of the sample is, for a large part, arbitrary, and so would be the gray level gradient at the border. Based on a previous segmentation, the proposed procedure isolates the role of the border and allows for tuning its weight. The respective variation of the two residual norms with k_b is a natural way to fine-tune this parameter.

In the following, $k_b = 0.25$ was empirically chosen, providing a good balance of the two contributions.

3.4. IDVC with Tikhonov regularization and trust region

In order to further improve the conditioning of the IDVC Hessian matrix $[H]$, a Tikhonov regularization is introduced when solving Equation 9. The new minimization problem is

$$\left([H_{\text{tot}}] + k_{\text{Tikh}}\lambda_{\text{I}}[I]\right)\{\delta p\} = \{b_{\text{tot}}\} + k_{\text{Tikh}}\lambda_{\text{I}}\left(\{p_{\text{ref}}\} - \{p\}\right) \tag{11}$$

where λ_{I} is the first eigenvalue of $[H_{\text{tot}}]$, $[I]$ is the identity matrix and k_{Tikh} is the regularization parameter. This regularization penalizes large deviations of the parameters from a reference set $\{p_{\text{ref}}\}$. In practice, $\{p_{\text{ref}}\}$ is the initial set, and $k_{\text{Tikh}} = 10^{-4}$. This regularization ensures that the actual material parameters do not differ too much from the initial ones. Let us stress that carbon-carbon properties are issued from previous experimental campaigns and are well-known.

A trust region was also implemented. It limits the maximal relative variation of any parameter of $\{p\}$ to 10% of its value while maintaining the research direction. This trust region slows down the convergence slightly, but it is active only during a few first iterations and has a strong stabilizing effect.

4. Identification procedure

The identification procedure is divided into three successive steps:

- the determination of the rigid body motion of the sample all along the test; this determination is performed thanks to a simple Integrated-DVC

algorithm, expressing the displacement field using only the six rigid-body-motion shape functions;

- the fine identification of macro-scale material parameters by IDVC;
- the identification of the best interface position between the two phases by IDVC.

The rigid body motion does not result from thermal loading. Therefore, it should not be considered free during the identification. The IDVC residual is computed with respect to the parameters $\{p\}$ and the measured rigid body motion $\boldsymbol{u}_{\mathrm{RBM}}$

$$\rho(\boldsymbol{x}, \{p\}) = f(\boldsymbol{x}) - g(\boldsymbol{x} + \boldsymbol{u}(\{p\}) + \boldsymbol{u}_{\mathrm{RBM}}) \tag{12}$$

The knowledge of material properties is not perfect. The initial guess of glass-carbon properties is rather approximate. A fine identification of those properties is thus a mandatory preliminary step. Only then can the best mechanically-based position of the interface be identified.

4.1. Computation of the sensitivity fields

The sensitivity fields $\{S_i\}$ are computed numerically using Abaqus and the model presented in Section 2. The displacement boundary conditions are applied to ensure that the problem is isostatic. Two thermal loading steps are modeled (120°C and -40°C), and the temperature is assumed to be homogeneous inside the sample. The magnitude of the displacement field is very small, and the sensitivities must be computed carefully. If the material models are linear, the discontinuity of properties at the interface induces geometrical nonlinearities. In Abaqus, a convergence criterion based on the displacement field correction norm is chosen. It is tuned to enforce at least two iterations.

4.2. Identification of material parameters

The initial homogenized thermomechanical properties of the two phases are not exact. They are determined finely using the presented IDVC procedure.

In the considered test, the loading is purely thermal. For the considered temperature range, the material is assumed to have an orthotropic linear thermoelastic behavior with properties that do not vary with temperature. The model then contains twelve material parameters by phase (nine parameters for the orthotropic elastic behavior and three coefficients of thermal expansion). The initial values of material parameters are listed in Table 1. The lack of force (or force-like) measurement induces an indetermination: all the moduli are accessible only up to a multiplicative factor. This indetermination is solved by fixing one modulus to a conventional value. The warp Young's modulus (E_{11}) of the carbon-carbon was chosen because it is the best-determined parameter from conventional experiments. As the displacements induced by the thermal loading are very small, the sensitivity to the Poisson's ratios is low. They have a minor influence on the kinematics in this particular experiment and cannot be accurately determined. The precision of their initial guess, though, does not influence the quality of the identification of the other parameters.

The material parameters have different natures and magnitudes. They are normalized in a prior stage so that an infinitesimal variation of normalized parameters induces sensitivity fields of the same order of magnitude [26]. Each sensitivity field is computed numerically by subtracting the results of the finite-element analysis with reference parameters to the ones perturbing the considered parameter.

4.3. Identification of the position of the interface

It was chosen to describe the interface using a conformal finite-element mesh. The topology of the mesh is preserved while moving the position of the interface, *i.e.* the interface nodes remain the same only their positions change. The positions of the other nodes of the perturbed mesh are obtained by linearly interpolating the interface node displacements on the mesh thickness. As the correction of the interface position is expected to be small, this simple description is sufficient and does not induce distortion. Furthermore, the interface can move continuously. However, updating the mesh requires some additional

steps. Indeed, the sensitivity field is the difference between the displacement fields resulting from two finite-element computations on two different meshes. An interpolation is needed to express the displacement field with the perturbed parameter on the nodes of the reference mesh. The shape functions of the perturbed mesh are used for interpolation to avoid large interpolation errors. Figure 4 shows an example of the sensitivity computation. In this illustration, the "infinitesimal increment" was exaggerated to make the mesh deformation visible in plain sight. The actual value of the increment used for identification is ten times lower.

From a mathematical point of view, adding geometrical parameters to the set of parameters to identify is transparent. However, in terms of implementation, updating the mesh has significant implications. Mesh shape functions have to be computed at each iteration to update the correlation Hessian matrix $[M]$ (Eq. 4).

5. Results

5.1. Elasticity hypothesis

The initial and last steps of the experiment (return to room temperature) can be used to confirm that the material remains in the elastic domain over the entire temperature excursion. The gray level residual ρ between the volumes at those two steps considering only the rigid body motion should be pure noise. In practice, this field does not display a perfect white Gaussian noise. Some tomographic artifacts, such as ring artifacts close to the axis of rotation and beam hardening, are still discernible (Fig. 5). In contrast, the texture of the sample vanishes on the residual, in agreement with the expectation of no remanent deformation between those two steps, *i.e.* that it remains in the elastic domain.

On the residual of this loading step, the artifacts remain sufficiently small to use a uniform standard deviation, σ_ρ, of this residual to estimate of the noise level of the tomography $\sigma_f = \sigma_\rho/\sqrt{2} = 1.05\%$ (percentage of the dynamic range

of f). This small noise level indicates that the tomographic images are of very good quality. This noise level is used to compute the uncertainty on identified parameters displayed in Table 1.

5.2. Identification of material properties

Table 1 sums up the identified material parameters. The initial parameters of the carbon-carbon phase were determined from an experimental study of the monophasic material — in the thickness direction, the identified values of E_{33} and k_{33} differ significantly from their initialisation. This could result from a poor determination by the traditional method or a lack of representativeness of the monophasic sample in this direction. In contrast, the initial properties of the glass-carbon phase were determined from the properties of carbon-carbon by changing the properties in the warp direction. This initial guess does not consider the phenomena related to the polymerisation at high temperature of the composite which could induce, traction in one phase (making it stiffer) and contraction in the other (softening it). It is questionable and explains why, for this phase, the initialization is quite far from the identified parameters (Fig. 6), namely for the Young's modulus in the direction aligned with the glass tows. Although the displacement field magnitude is low, the error in the displacement field is clearly visible in the residual field (Fig. 7). That poor initial guess mainly explains the substantial parameter variation during the identification.

The uncertainty displayed in Table 1 corresponds to the uncertainty resulting from the noise of the images if all parameters are considered independently (more details about the computation and typical interpretation of those uncertainties can be found in [26]).

5.3. Determination of the best interface

Figure 5a displays the initial and identified positions of the interface. The initial interface was determined from topological features: the respective number of layers of each phase in the fabric. The identified one is based on a mechanical criterion. As the weaving is wavy, those interfaces cross some glass yarns. The

identified interface position at $0.35h$ (h being the thickness of the sample) is close to the initial one at $3/8 = 0.375h$. The correction is of about 150 µm.

6. Discussion

6.1. On the interest of IDVC

The studied displacement fields have a very low amplitude with respect to the sample dimension and the voxel size of the tomography. IDVC is particularly well suited in that sense. *Classical* DVC, using the same mesh as IDVC, provides a very noisy displacement field. Its amplitude is of the same order as its uncertainty. Moreover, the non-homogeneous texture of the sample leads to poor robustness.

A more conventional approach, DVC followed by Finite Element Model Updating (FEMU) [31, 32], was also tested but did not yield satisfactory results. The full kinematics cannot be determined with sufficient accuracy on a mesh fine enough to describe the interface — with a coarser mesh, the kinematic is not well captured. The ill-posedness of the DVC problem tends to increase the noise in the areas where the texture is low to the extent that the displacement field diverges at some points. This error is conveyed to the parameters during the identification. The FEMU algorithm does not converge or converges towards unphysical parameters values, with large final residuals. IDVC allows bypassing this problem by reducing the number of degrees of freedom. This reduction allows for the parameter determination with the low uncertainties listed in Table 1.

6.2. Computational efficiency

Each update of the material parameters takes 4 min on a Linux work station. The most time-expensive step is the computation of the sensitivity fields. The 18 Abaqus computations are parallelized on 18 CPUs (Intel(R) Xeon(R) Silver 4116 CPU (Skylake)@2.10GHz). The number of parameters has thus no impact on the computation time. Given that, during the identification of material

parameters, the mesh does not change, the DVC Hessian matrix $[M]$ does not need updating and can be computed beforehand.

An interface position updating iteration takes 7.8 min. This long duration is due to the interpolation performed during the computation of the sensitivity field and the update of the DVC Hessian matrix (as the mesh changes, the shape functions, $\boldsymbol{\varphi}$, change at each iteration).

The convergence is reasonably fast: 16 iterations for the material parameter identification and 33 for the determination of the interface position. The trust region increases this time cost but fosters a smooth monotonic evolution of the residual norm r (Fig. 8). Including pre-processing (mainly the loading of the images), material parameter identification takes about 1.4 h whereas interface updating takes about about 5 h.

As expected, the residual is stationary before reaching the convergence criterion ($\|\delta p\| < 1$) (Fig. 8).

6.3. Mechanically-based interface

The *mechanically-based* interface is the one that provides the best description of the measured kinematics. The high sensitivity to the interface position (Fig. 4) shows that this position has a first-order impact on the deformation of the sample. Even a small correction of this position improves the model. The mechanically-based interface is not necessarily far from the geometrically-based one, as this is the case here. However, the mechanically-based interface is less arbitrary and intrinsically takes into account the modeling choices.

In this case, all the material properties of the two phases of the material were not well-known before the identification. The coupling between material and geometrical parameters causes a non-uniqueness of the solution. If the interface position identification were performed before the material one, it would not be the same. The gap between the initial and identified one would have been larger.

7. Conclusion

An in-situ thermal experiment is processed by IDVC to identify the material and geometrical parameters of a material modeled as macroscopically biphasic. Given that the magnitude of the measured displacement field is close to the conventional DVC measurement uncertainty, IDVC is thus particularly well-suited for this problem. The strain level is very low, and strain gauge measurements are impractical due to the heterogeneity at the weaving scale. IDVC also proves to be more robust to noise than FEMU coupled to DVC and provides accurate identification of the material and geometrical parameters of the model. A regularization procedure based on the sample boundaries was implemented to balance the heterogeneity of the texture contrast in the tomographic images.

Material parameters' identification is required because they are not well-known *a priori*. The mechanically-based position of the interface between the two phases is estimated accuratly. The study of the residual fields shows that the proposed homogenized model provides a good description of the thermomechanical behavior of the sample.

Further work will focus on more complex interface geometries, keeping in mind that it should remain relatively smooth to preserve the simplicity of the homogenized model, which in essence, ignores the small-scale details of the composite. Such models are used to simulate the manufacturing process of complex parts, *e.g.* fan blade. As the deformation of the part is constrained, the macroscale heterogeneity induces a residual stresses that impact the mechanical strength. The accuracy of the determination of the shape and the position of the interfaces affects the apparent mechanical strength.

Acknowledgement

This project is funded by Safran Aircraft Engines. It is a pleasure to acknowledge Yannick Yasothan, Keerthi-Krishna Parvathaneni, Rafael Vargas and Xuyang Chang for fruitful discussions.

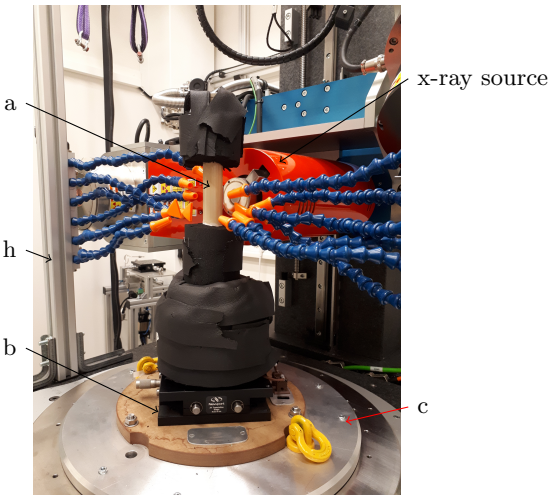

(a)

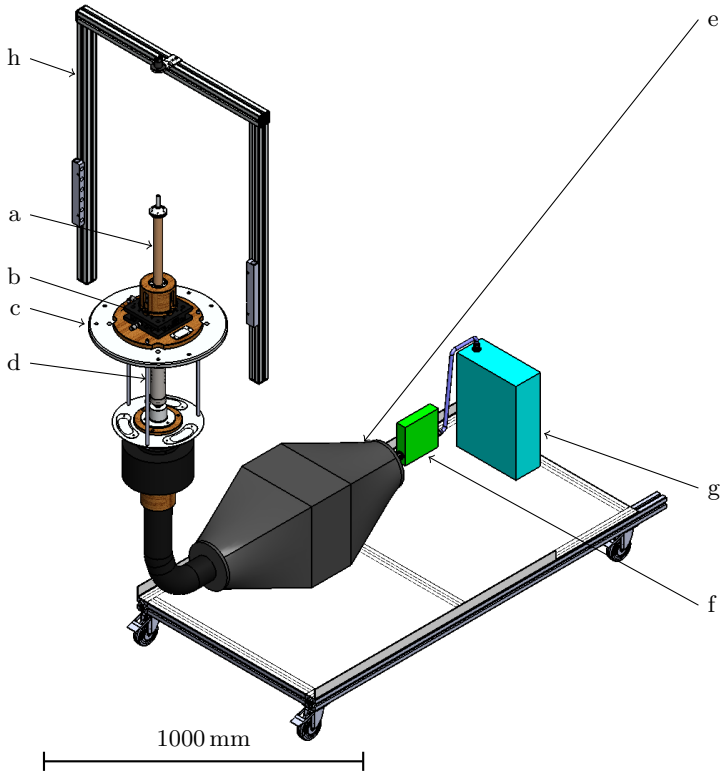

(b)

Figure 2: In-situ heating-cooling device: (a) inside the tomograph, (b) CAD. The temperature inside the chamber **a** varies from −40°C to 120°C during the experiment. The tubular chamber is in PEEK (PolyEther Ether Ketone). Its diameter is 34 mm and its thickness, 2 mm. The chamber is fixed to the rotating stage **c** through a hollow xy stage **b**. During hot experiments, air is heated thanks to the heating tube **d**, in parallel the surrounding of the tube is cooled thanks to the air nozzle fixed to the gantry **h**. During cold experiments, the heat exchanger **e**, located under the tomograph table, is used. **f** and **g** are the piloting electrical cabinet.

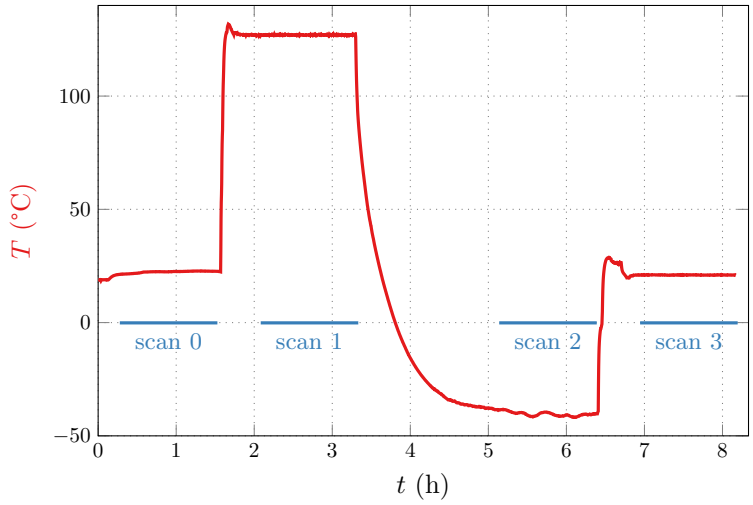

Figure 3: Thermal loading. A tomography (——) is acquired during each step. —— is the servo temperature measured at the air nozzle. The heating-cooling device is calibrated with a thermocouple before the experiment to ensure the desired temperature at the center of the tube.

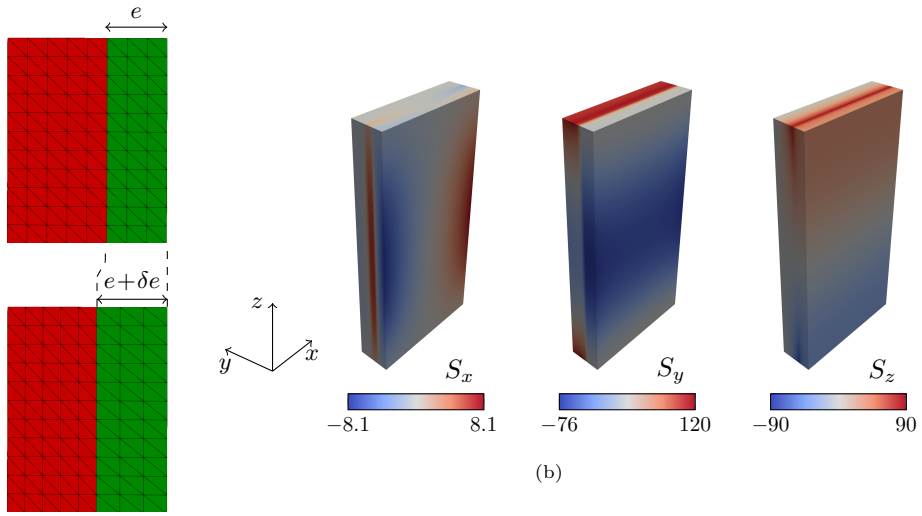

(a) (b)

Figure 4: Computation of the sensitivity of the position e of the interface. (a) The topology of the mesh (number of elements in each phase) stays unchanged. Only the position of the interface is incremented by δe. The sensitivity field, $\boldsymbol{S} = \{S_x, S_y, S_z\}$ (µm), for the heating step (b) is the induced displacement $\boldsymbol{u}(e + \delta e) - \boldsymbol{u}(e)$. A significant increment has been chosen for the figure so that the mesh changes are visible.

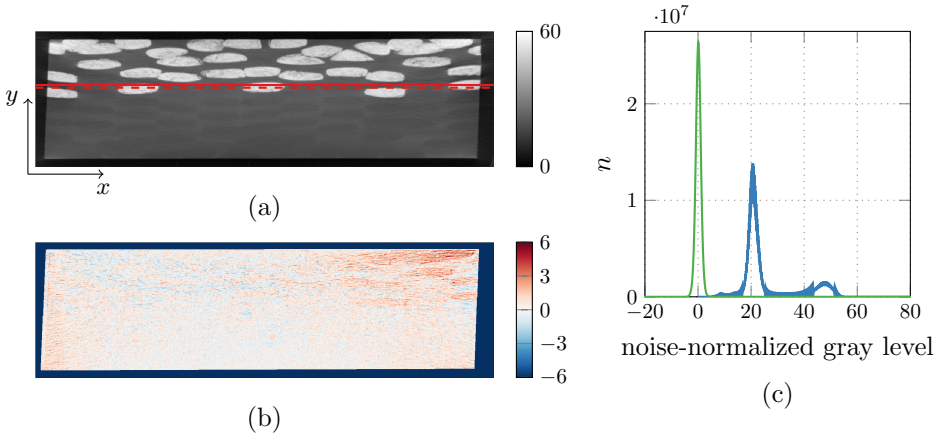

Figure 5: Mid xy-slice of the reference volume (a) and of the residual field at the return to 20°C step (b), (c) histograms of the reference volume (in blue, ——) and of the residual field (in green, ——) in the whole region of interest. The gray levels are normalized by the noise level σ_ρ. In (a), the initial interface position ($3/8h = 0.375h$, - - -) and the identified one ($0.35h$, ——) are drawn (h being the thickness of the sample).

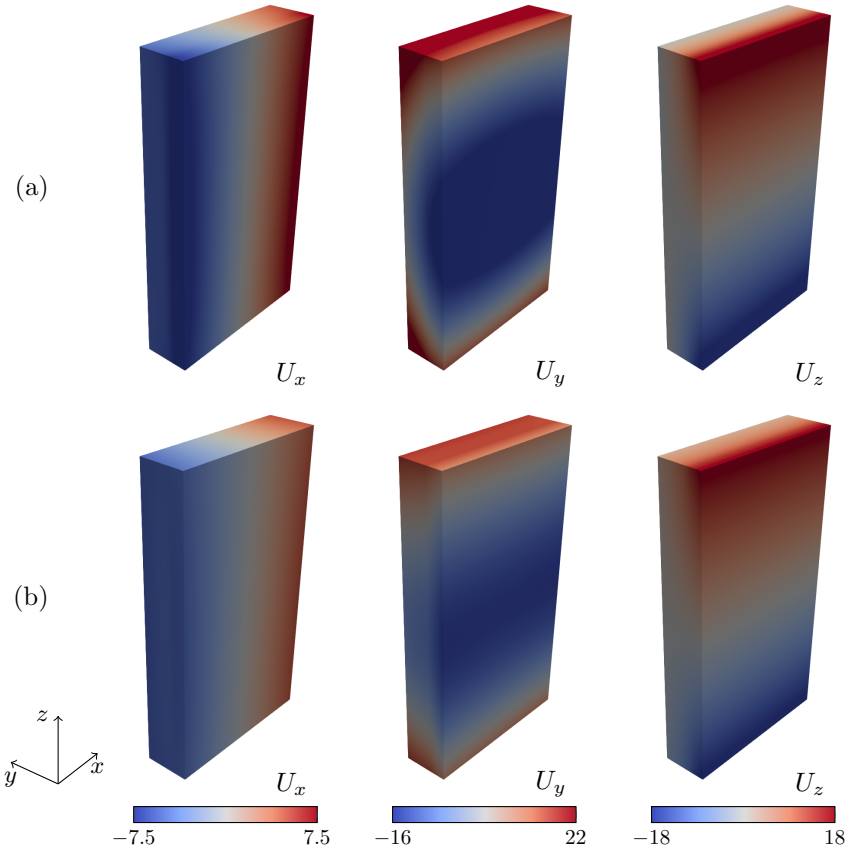

Figure 6: Displacement field (µm) induced by the heating step: (a), with the initial parameters and (b) with the identified ones.

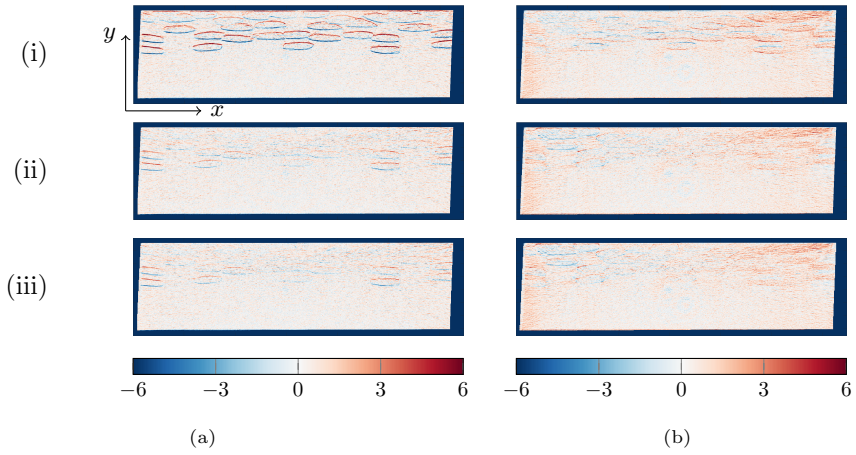

Figure 7: Evolution of the residual field in the mid-xy slice (gray level normalized by the noise level). (a) first loading step (120°C) and (b) second loading step (−40°C). (i) initial residual (after rigid body motion correction); (ii) residual after the identification of material parameters; (iii) residual after identification of the position of the interface.

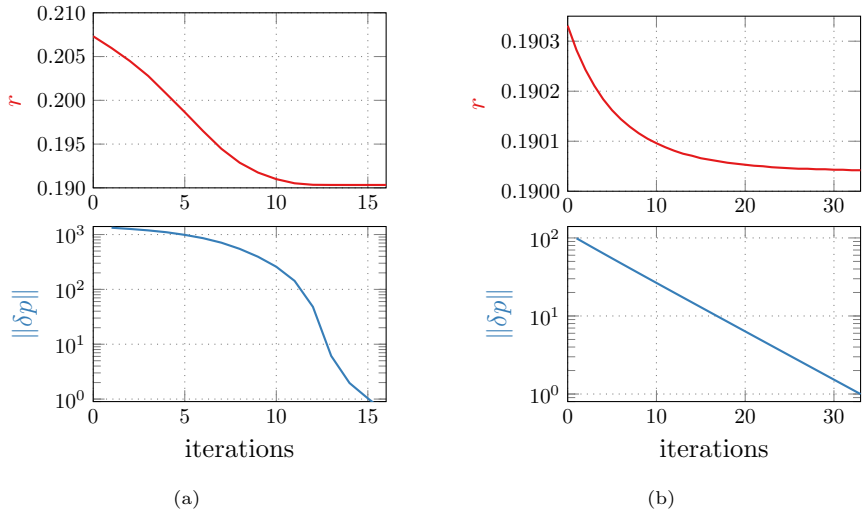

Figure 8: Evolution of convergence criteria during the identification: (a) identification of material parameters; (b) identification of the position of the interface. r is the root mean square of the residual field $\rho(\boldsymbol{x})$. Convergence is reached when $\|\delta p\| < 1$, at this time the residual is already stationary.

References

[1] J. J. Andrew, S. M. Srinivasan, A. Arockiarajan, H. N. Dhakal, Parameters influencing the impact response of fiber-reinforced polymer matrix composite materials: A critical review, Compos. Struct. 224 (2019) 111007. doi:10.1016/j.compstruct.2019.111007.

[2] F. Ahmad, N. Yuvaraj, P. K. Bajpai, Effect of reinforcement architecture on the macroscopic mechanical properties of fiberous polymer composites:A review, Polymer Compos. 41 (6) (2020) 1–17. doi:10.1016/j.compstruct.2019.111007.

[3] K. M. F. Hasan, P. G. Horváth, T. Alpár, Potential fabric-reinforced composites: a comprehensive review, J. Mater. Sc. 56 (26) (2021) 14381–14415. doi:10.1007/s10853-021-06177-6.

[4] Y. Swolfs, L. Gorbatikh, I. Verpoest, Fibre hybridisation in polymer composites: A review, Compos. Part A 67 (2014) 181–200. doi:10.1016/j.compositesa.2014.08.027.

[5] M. Jalalvand, G. Czél, M. R. Wisnom, Damage analysis of pseudo-ductile thin-ply ud hybrid composites – a new analytical method, Compos. Part A 69 (2015) 83–93. doi:10.1016/j.compositesa.2014.11.006.

[6] A. Enfedaque, J. Molina-Aldareguía, F. Gálvez, C. González, J. LLorca, Effect of glass fiber hybridization on the behavior under impact of woven carbon fiber/epoxy laminates, Journal of Composite Materials 44 (25) (2010) 3051–3068. doi:10.1177/0021998310369602.

[7] V. Infante, J. Madeira, R. B. Ruben, F. Moleiro, S. T. de Freitas, Characterization and optimization of hybrid carbon–glass epoxy composites under combined loading, J. Compos. Mater. 53 (18) (2019) 2593–2605. doi:10.1177/0021998319834673.

[8] B. Yang, Z. Wang, L. Zhou, J. Zhang, W. Liang, Experimental and numerical investigation of interply hybrid composites based on woven fabrics and

pcbt resin subjected to low-velocity impact, Compos. Struct. 132 (2015) 464–476. doi:10.1016/j.compstruct.2015.05.069.

[9] D. Zhang, A. M. Waas, C.-F. Yen, Progressive damage and failure response of hybrid 3d textile composites subjected to flexural loading, part i: Experimental studies, Int. J. Solids Struct. 75-76 (2015) 309–320. doi:10.1016/j.ijsolstr.2015.06.034.

[10] S. Ahmed, X. Zheng, L. Yan, C. Zhang, X. Wang, Influence of asymmetric hybridization on impact response of 3d orthogonal woven composites, Compos. Sci. Technol. 199 (2020) 108326. doi:10.1016/j.compscitech.2020.108326.

[11] Q. Liang, J. Liu, X. Wang, X. Liu, D. Zhang, K. Qian, Flexural progressive failure mechanism of hybrid 3d woven composites: Combination of x-ray tomography, acoustic emission and digital image correlation, Composite Structures 280 (2022) 114894. doi:10.1016/j.compstruct.2021.114894.

[12] S. V. Lomov, D. S. Ivanov, I. Verpoest, M. Zako, T. Kurashiki, H. Nakai, S. Hirosawa, Meso-fe modelling of textile composites: Road map, data flow and algorithms, Compos. Sci. Technol. 67 (9) (2007) 1870–1891. doi:10.1016/j.compscitech.2006.10.017.

[13] J. Bénézech, G. Couégnat, Variational segmentation of textile composite preforms from X-ray computed tomography, Compos. Struct. 230 (2019) 111496. doi:10.1016/j.compstruct.2019.111496.
URL https://doi.org/10.1016/j.compstruct.2019.111496

[14] D. Durville, I. Baydoun, H. Moustacas, G. Périé, Y. Wielhorski, Determining the initial configuration and characterizing the mechanical properties of 3D angle-interlock fabrics using finite element simulation, Int. J. Solids Struct. 154 (2018) 97–103. doi:10.1016/j.ijsolstr.2017.06.026.
URL https://doi.org/10.1016/j.ijsolstr.2017.06.026

[15] R. Gras, H. Leclerc, F. Hild, S. Roux, J. Schneider, Identification of a set of macroscopic elastic parameters in a 3d woven composite: Uncertainty analysis and regularization, I. J. Solids Struct. 55 (2015) 2–16. doi:10.1016/j.ijsolstr.2013.12.023.

[16] C. J. Peel, P. J. Gregson, Design requirements for aerospace structural materials, Springer Netherlands, Dordrecht, 1995, pp. 1–48. doi:10.1007/978-94-011-0685-6_1.

[17] C.-C. Chiu, Determination of the elastic modulus and residual stresses in ceramic coatings using a strain gage, J. Am. Ceram. Soc. 73 (7) 1999–2005. doi:https://doi.org/10.1111/j.1151-2916.1990.tb05258.x.

[18] H. A. Bruck, S. R. McNeill, M. A. Sutton, W. H. Petters, Digital Image Correlation Using Newton-Raphson Method of Partial Differential Correction, Exp. Mech. 29 (1989) 261–267. doi:10.1007/BF02321405.

[19] R. Gras, H. Leclerc, S. Roux, S. Otin, J. Schneider, J.-N. Périé, Identification of the out-of-plane shear modulus of 3d woven composite, Exp. Mech. 53 (2012) 719–730. doi:10.1007/s11340-012-9683-4.

[20] K. B. Bay, T. S. Smith, D. P. Fyhrie, M. Saad, Digital Volume Correlation: Three-dimensional Strain Mapping Using X-ray Tomography, Exp. Mech. 39 (3) (1999) 217–226. doi:10.1007/BF02323555.

[21] S. Roux, F. Hild, P. Viot, D. Bernard, Three-dimensional image correlation from X-ray computed tomography of solid foam, Compos. Part A 39 (8) (2008) 1253–1265. doi:10.1016/j.compositesa.2007.11.011.

[22] A. Buljac, C. Jailin, A. Mendoza Quispe, J. Neggers, T. Taillandier-Thomas, A. Bouterf, B. Smaniotto, F. Hild, S. Roux, Digital volume correlation: Review of progress and challenges, Exp. Mech. 58 (5) (2018) 661–708. doi:10.1007/s11340-018-0390-7.

[23] S. Roux, F. Hild, Stress intensity factor measurements from digital image correlation: Post-processing and integrated approaches, Int. J. Fract. 140 (2006) 141–157. doi:10.1007/s10704-006-6631-2.

[24] S. Roux, F. Hild, Optimal procedure for the identification of constitutive parameters from experimentally measured displacement fields, Int. J. Solids Struct. 184 (2020) 14–23. doi:10.1016/j.ijsolstr.2018.11.008.

[25] H. Leclerc, J.-N. Périé, S. Roux, F. Hild, Integrated digital image correlation for the identification of mechanical properties, in: A. Gagalowicz, W. Philips (Eds.), Computer Vision/Computer Graphics CollaborationTechniques, Springer Berlin Heidelberg, Berlin, Heidelberg, 2009, pp. 161–171. doi:10.1007/978-3-642-01811-4_15.

[26] L. Turpin, S. Roux, J. Bénézech, G. Couégnat, A. King, O. Caty, S. Denneulin, M. Éric, Quantitative thermo-mechanical characterisation of 3D-woven SiC/SiC composites from in-situ tomographic and thermographic imaging, Compos. Struct. 307 (2023) 116626. doi:10.1016/j.compstruct.2022.116626.

[27] A. Dasgupta, R. Agarwal, S. Bhandarkar, Three-dimensional modeling of woven-fabric composites for effective thermo-mechanical and thermal properties, Composites Science and Technology 56 (3) (1996) 209–223. doi:https://doi.org/10.1016/0266-3538(95)00111-5.

[28] Z. Hu, R. Karki, Prediction of mechanical properties of three-dimensional fabric composites reinforced by transversely isotropic carbon fibers, Journal of Composite Materials 49 (12) (2015) 1513–1524. doi:10.1177/0021998314535960.

[29] F. Hild, S. Roux, Digital image correlation: From displacement measurement to identification of elastic properties — A Review, Strain 42 (2006) 69–80. doi:10.1111/j.1475-1305.2006.00258.x.

[30] L. Turpin, S. Roux, O. Caty, S. Denneulin, Coupling tomographic and thermographic measurements for in-situ thermo-mechanical tests, Meas. Sci. Technol. 32 (2021) 035401. doi:10.1088/1361-6501/abcc9f.

[31] C. Farhat, F. M. Hemez, Updating finite element dynamic models using an element-by-element sensitivity methodology, AIAA Journal 31 (9) (1993) 1702–1711. doi:10.2514/3.11833.

[32] R. Vargas, R. Canto, B. Smaniotto, F. Hild, Calibration of cohesive parameters for a castable refractory using 4d tomographic data and realistic crack path from in-situ wedge splitting test, J. Eu. Ceram. Soc. 43 (2) (2023) 676–691. doi:10.1016/j.jeurceramsoc.2022.09.040.